*remote sensing*

MDPI

*Article*

# Coseismic Rupture Behaviors of the January and March 2022 $M_W$ > 5.5 Hala Lake Earthquakes, NE Tibet, Constrained by InSAR Observations

**Jiuyuan Yang [1], Caijun Xu [1,2,3,*] and Yangmao Wen [1,2]**

[1] School of Geodesy and Geomatics, Wuhan University, Wuhan 430079, China
[2] Key Laboratory of Geospace Environment and Geodesy, Ministry of Education, Wuhan University, Wuhan 430079, China
[3] Hubei Luojia Laboratory, Wuhan 430079, China
* Correspondence: cjxu@sgg.whu.edu.cn

**Abstract:** On 23 January and 25 March 2022, two $M_W$ > 5.5 Hala Lake earthquakes characterized by right-lateral strike-slip faulting occurred around the Elashan Fault in Northeastern Tibet, marking the two largest events since the 1927 $M_W$ 6.2 Hala Lake earthquake. Since no surface rupture related to the two earthquakes has been reported, the seismogenic faults and coseismic rupture behaviors of the two events are still unknown. The occurrence of the two events provides a rare opportunity to gain insight into the seismogenic structure and rupture behavior of the less studied region, further helping us accurately evaluate the regional seismic hazard. Here, we first exploit Interferometric synthetic aperture radar (InSAR) data to obtain the coseismic deformation associated with the two earthquakes and then invert for the fault geometry and detailed coseismic slip of the two events. Coseismic modeling reveals that the January and March 2022 earthquakes ruptured two buried west-dipping moderate-angle and high-angle right-lateral strike-slip faults, respectively. Most of the slip of the January event occurred at depths from 1.7–7.6 km, while the majority of the slip associated with the March event occurred at depths from 2.5–10 km, which may have been restricted by the intersections between the January and March Hala Lake seismogenic faults. By a comprehensive analysis of the coseismic inversions, stress changes, and early postseismic signal, we suggest that the significant fault dip difference (~30°), highlighting a fault segmentation, stops the rupture propagation from one fault segment to another and that fluid migration may encourage the restart of the rupture of the later event, which requires further investigation. Moreover, Coulomb stress modeling shows stress loading on the eastern segment of the Daxueshan–Shule Fault and the northern segment of the Elashan fault, which we should pay more attention to.

**Keywords:** Hala Lake earthquake; InSAR; coseismic deformation; buried strike-slip fault; coulomb stress



**Citation:** Yang, J.; Xu, C.; Wen, Y. Coseismic Rupture Behaviors of the January and March 2022 $M_W$ > 5.5 Hala Lake Earthquakes, NE Tibet, Constrained by InSAR Observations. *Remote Sens.* **2023**, *15*, 1124. https://doi.org/10.3390/rs15041124

Academic Editors: Chisheng Wang, Bochen Zhang, Chuanhua Zhu and Biao Lu

Received: 7 January 2023
Revised: 6 February 2023
Accepted: 16 February 2023
Published: 18 February 2023



## 1. Introduction

On 23 January 2022 (UTC Time 2:21), an $M_W$ 5.6 shallow earthquake, which was followed by one $M_S$ > 3.0 aftershock, occurred ~13 km northwest of the Hala Lake in Qinghai Province, China (Figure 1). On 25 March 2022 (UTC Time 16:21), a much larger shallow earthquake with $M_W$ 5.7—marking the largest event around the Hala Lake for the last 95 years—occurred ~7 km northwest of the January 2022 Hala Lake event (Figure 1). After the March 2022 earthquake, a total of 11 $M_S$ > 3.0 aftershocks was recorded in the following 45 days from 25 March to 12 May 2022. As the epicenters of the two Hala Lake earthquakes were located in No Man's Land, the events caused no casualties. The focal mechanism solutions from the Global Centroid Moment Tensor (GCMT; https://www.globalcmt.org/, accessed on 1 January 2023) and the United States Geological Survey (USGS; https://www.usgs.gov/, accessed on 1 January 2023) (Tables 1 and 2) reveal that the January and March 2022 Hala Lake earthquakes activated two nearly NS-striking

moderate-angle and high-angle right-lateral strike-slip faults, respectively. The occurrence of the January and March 2022 events offers an important opportunity to improve our knowledge of the seismogenic structure of the regional active fault with modern datasets (e.g., InSAR). So far, no related geodetic studies about the two Hala Lake earthquakes have been published. The detailed InSAR study of the two events can contribute to a deeper understanding of the regional seismogenic mechanism and tectonic deformation. Moreover, a coinstantaneous multi-fault rupture in a single earthquake often results in a higher hazard than that induced by the delayed rupture of multiple faults in an earthquake doublet or a seismic sequence, which spans a long period of days to months [1,2]. Studying the delayed rupture (about two months apart) between the two Hala Lake events can also enhance our understanding of the controlling factors for the kinematic evolution of rupture during an earthquake doublet or a seismic sequence, which will help us accurately evaluate the regional seismic hazard.

**Table 1.** Source parameters of the 23 January 2022 $M_W$ 5.6 Hala Lake earthquake.

| Model | Lon/° | Lat/° | Strike/° | Dip/° | Rake/° | Length/km | Depth/km | Slip/m | $M_W$ |
|---|---|---|---|---|---|---|---|---|---|
| USGS | 97.34 | 38.46 | 171 | 60 | −168 | - | 10 | - | 5.6 |
| GCMT | 97.39 | 38.52 | 169 | 74 | −173 | - | 18.4 | - | 5.6 |
| U-S-model | $97.37^{+0.24km}_{-0.24km}$ | $38.46^{+0.43km}_{-0.43km}$ | $172.42^{+4.3}_{-4.3}$ | $61.8^{+2.3}_{-2.3}$ | $-175.1^{+4}_{-4}$ | $7.4^{+0.28}_{-0.28}$ | $1.9^{+0.15}_{-0.15}$ | $0.15^{+0.02}_{-0.02}$ | 5.53 |

Notes: U–S model represents the uniform slip model. The location (longitude and latitude) of the uniform slip model indicates the center of up-dip surface projection of the rupture fault plane. Depth shows the midpoint of the upper boundary of the uniform fault plane.

**Table 2.** Source parameters of the 25 March 2022 $M_W$ 5.7 Hala Lake earthquake.

| Model | Lon/° | Lat/° | Strike/° | Dip/° | Rake/° | Length/km | Depth/km | Slip/m | $M_W$ |
|---|---|---|---|---|---|---|---|---|---|
| USGS | 97.29 | 38.54 | 352 | 90 | 172 | - | 10 | - | 5.7 |
| GCMT | 97.34 | 38.54 | 173 | 87 | −174 | - | 21.1 | - | 5.8 |
| U-S-model | $97.34^{+0.18km}_{-0.18km}$ | $38.50^{+0.25km}_{-0.25km}$ | $176^{+2.2}_{-2.2}$ | 87 (Fixed) | $-165^{+4.1}_{-4.1}$ | $5.3^{+0.6}_{-0.6}$ | $2.5^{+0.3}_{-0.3}$ | $0.35^{+0.08}_{-0.08}$ | 5.71 |

Notes: All the abbreviations and symbols in Table 2 are the same as those in Table 1, but for the March 2022 Hala Lake earthquake.

InSAR data, characterized by high precision and high resolution [3,4], have been widely applied to investigate crustal deformation caused by the seismic cycle [5–8] since its successful use to the 1992 Mw 7.3 Landers earthquake [4]. As the first two seismic events detected by InSAR in the Hala Lake area, it is meaningful to derive the interferometric phase associated with the Hala Lake earthquakes so as to gain insight into the regional seismogenic stucture and seismic hazard. In this study, we first make use of Sentinel-1 SAR data to image the coseismic surface displacements of the January and March 2022 Hala Lake earthquakes. Then, we utilize the coseismic observations to invert for the fault geometry and detailed coseismic slip of the two earthquakes. Subsequently, we explore the effect of the January 2022 $M_W$ 6.7 Menyuan earthquake on the two Hala Lake earthquakes and analyze the possible causes for the termination and restart of the slip during the two similar magnitudes and temporally separated Hala Lake earthquakes. Lastly, the influence of the coseismic coulomb stress changes caused by the two Hala Lake events on the surrounding faults is calculated in order to assess the regional seismic hazards.

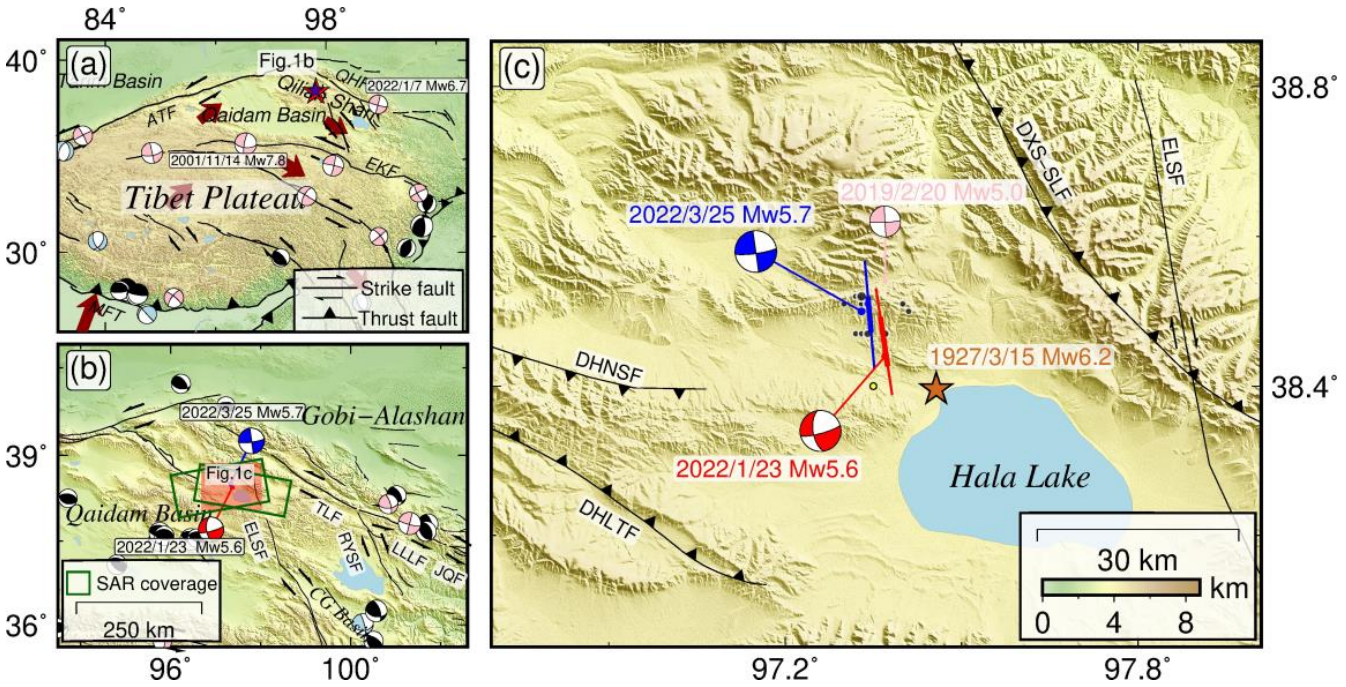


**Figure 1.** (**a**) Tectonic background of Tibet plateau. Large dark red arrows show the plate motion [9]. ATF: Altyn Tagh fault; EKF: East Kunlun fault; MFT: Main frontal thrust; QHF: Qilian-Haiyuan fault; Red and blue stars represent the epicenters of the January and March 2022 Hala Lake earthquakes, respectively. (**b**) Tectonic map of the NE Tibet. TLF: Tuolaishan fault; JQF: Jinqianghe fault; LLLF: Lenglongling fault; ELSF: Elashan fault; RYSF: Riyueshan fault; CG basin: Chaka-Gonghe basin. (**c**) Tectonic setting around the two 2022 Hala Lake earthquakes. Thin red and blue lines indicate the coseismic fault traces of the January and March 2022 Hala Lake earthquakes, respectively, from the slip distribution models, while the thick red and blue lines superimposed on the thin lines depict the coseismic fault traces of the January and March events, respectively, from the uniform slip models. Yellow circle represents the $M_S$ > 3.0 aftershock after the January 2022 event, whereas black circles are $M_S$ > 3.0 aftershocks occurred between 26 March and 13 May 2022. All aftershocks are acquired from the China Earthquake Networks Center (CENC; https://www.cenc.ac.cn/, accessed on 1 January 2023). DHLTF: Dahaletenghe fault; DHNSF: Danghenanshan fault; DXS-SLF: Daxueshan-shule fault. Faults are acquired from Institute of Geology, China Earthquake Administration (https://www.eq-igl.ac.cn/, accessed on 1 January 2023). Black, pink, and light-blue beach balls denote the focal mechanisms of historical thrust, strike-slip and normal earthquakes, respectively, from GCMT (Thereinto, beach balls in (**a**,**b**) represent $M_W$ > 6.5 and $M_W$ > 5.5 earthquakes, respectively, while those in Figure 1c indicate $M_W$ > 5.0 earthquake).

## 2. Tectonic Background

As the forefront of the northward expansion of the Tibet plateau moves towards the interior continent, the northeast margin of the Tibet Plateau characterized by strong tectonic activity has been suffering from the intensive shearing deformation since Late Quaternary due to the continuing collision between the Indian and Eurasian plates, thus developing many prominent strike-slip faults such as the nearly E-W-trending left-lateral strike-slip East Kunlun fault (EKLF), the Qilian–Haiyuan fault (QHF), the NW–SE-trending right-lateral strike-slip Elashan fault (ELSF) and Riyueshan fault (RYSF) ([10–12]; Figure 1a,b). These strike-slip faults are considered to play an important role in regulating the eastward motion of Tibet plateau relative to the Gobi–Alashan block (GAB) and to have frequent seismic activity (e.g., [13]). However, compared with that the 2001 $M_W$ 7.8 Kokoxili and 2022 $M_W$ 6.7 Menyuan earthquakes ruptured the large sinistral strike-slip EKLF and QHF, respectively ([14,15]; Figure 1a), the lack of recent $M_W$ > 5.5 moderate-to-large earthquakes occurred in the secondary dextral strike-slip faults such as the ELSF and RYSF (Figure 1b),

which hinders our understanding of the regional tectonic environment. As the tectonically active boundary between the Qaidam basin and Chaka–Gonghe basin, the ELSF consisting of several discontinuous subparallel NW–SE-trending right-stepping or left-stepping "en echelon" strike-slip fault segments have a length of ~200 km ([16]; Figure 1b). Its northern segment is especially considered to be characterized by some horsetail splay faults [17], which may be associated with the seismogenic faults of the January and March 2022 Hala Lake events. As the two largest earthquakes since the 1927 $M_W$ 6.2 Hala Lake earthquake (Figure 1c), the two 2022 Hala Lake earthquakes occurred around the northern segment of the ELSF, presenting a rare chance to gain insight into the regional tectonic deformation and seismogenic structure.

## 3. InSAR Observations

Benefitting from the short revisit period of Sentinel-1A satellite, we derive a rare chance to study the 2022 Hala Lake seismic sequence separately. Aiming at acquiring the coseismic deformation associated with the January and March 2022 Hala Lake earthquakes, we use the two-pass differential SAR interferometry method [18] to process six pairs of Sentinel-1 Single Look Complex SAR images (Tables 3–5) with a multi-looking factor of 2 by 10 along the azimuth and range directions on the basis of the Gamma software [19]. A 30 m digital elevation model and a power spectrum filter [20] are exploited to exclude the topographic contributions and filter the phase, respectively. Finally, we use the branch cut method [21] to unwrap the interferograms and further geocoded them to the WGS84 geographic coordinates. These things considered, in order to eliminate both the topography-correlated atmospheric delays and residual orbital errors, a linear function between the error phase, location, and elevation is estimated by the virtue of coseismic observations far from the major deformation area [22]. The continuous deformation fringe pattern of the coseismic interferograms (Figure 2a–d) implies that the coseismic rupture of the two earthquakes doesn't propagate to the surface. For the January 2022 Hala Lake earthquake, the ascending coseismic interferograms (Figure 2a) show two major lobe deformation areas with the southwest quadrant moving away from the satellite and the northwest quadrant moving towards the satellite, whereas the descending coseismic interferograms (Figure 2b) reveal three prominent lobe deformation areas with the southwest quadrant moving away from the satellite and the northwest and southeast quadrants moving towards the satellite. Such asymmetric deformation patterns exhibited in the ascending and descending interferograms (Figure 2a,b) indicate a predominantly dextral strike-slip motion. In addition, the deformation magnitude in the west is much larger than that in the east in the two interferograms, indicating a west-dipping seismogenic fault. For the March 2022 Hala Lake earthquake, the overall deformation pattern shown in the ascending and descending interferograms (Figure 2c,d) is generally similar to that of the January 2022 Hala Lake earthquake (Figure 2a,b). In particular, the deformation magnitude in the east is much larger than that in the west in the descending interferogram (Figure 2d), which is contrary to that in the ascending interferogram (Figure 2c), implying a nearly sub-vertical fault. Hence, taking into consideration the above descriptions, we suggest that one west-dipping and one nearly sub-vertical buried right-lateral strike-slip faults may be activated during the January and March 2022 Hala Lake earthquakes, respectively. The ranges of line-of-sight (LOS) displacements in the two ascending interferograms are −1.9 to 1.9 cm for the 23 January event (Figure 2e) and −3.0 to 1.2 cm for the 25 March event (Figure 2g), respectively, while the ranges of LOS displacements in the two descending interferograms are −1.2 to 0.7 cm for the 23 January event (Figure 2f) and −1.4 to 2.9 cm for the 25 March event (Figure 2h), respectively. In addition, we also acquired the coseismic interferograms associated with both the 23 January and 25 March events. The overall deformation exhibited in the ascending and descending interferograms (Figure 2m,o) is generally similar to that of any single Hala Lake event (Figure 2a–d) but has a more complex and larger deformation (Figure 2e–h,n,p). It should be noted that we do not use the total coseismic deformation to the geodetic inversion because solving for the geometries of multiple faults

simultaneously will result in trade-offs between fault parameters during the inversion [23]. Finally, to preliminarily assess the early postseismic deformation associated with the 23 January event, five Sentinel-1A ascending images spanning the time period from 27 January 2022 to 16 March 2022, and five descending images spanning the time period from 1 February 2022 to 21 March 2022, are also analyzed (Table 6). We processed all interferometric pairs in the same way as the coseismic interferogram and apply the MintPy package to process the following InSAR time series on the basis of the small baseline method [24–26]. Our preliminary postseismic displacement (Figure 3) highlights that the cumulative early postseismic is limited and can be ignored.

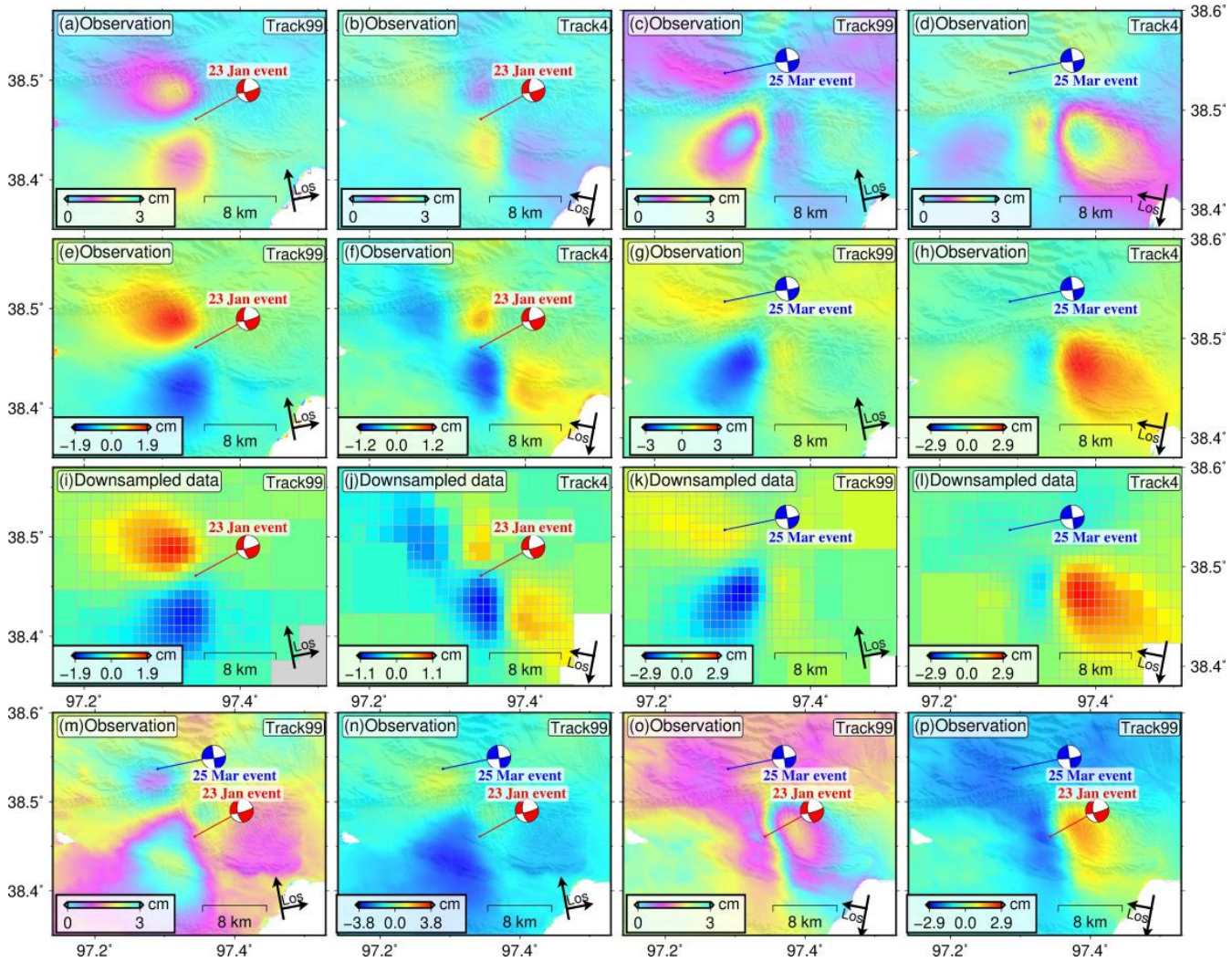


**Figure 2.** (**a**,**b**) are ascending and descending coseismic interferograms, respectively, covering the 23 January 2022 Hala Lake earthquake. (**e**,**f**) are corresponding coseismic displacements. (**i**,**j**) are corresponding down-sampled LOS displacement. (**c**,**d**) are ascending and descending coseismic interferograms, respectively, covering the 25 March 2022 Hala Lake earthquake. (**g**,**h**) are corresponding coseismic displacements. (**k**,**l**) are corresponding down-sampled LOS displacements. (**m**) is ascending coseismic interferograms covering the 23 January and 25 March 2022 Hala Lake earthquakes. (**n**) is corresponding coseismic displacements. (**o**) is descending coseismic interferograms covering the 23 January and 25 March 2022 Hala Lake earthquakes. (**p**) is corresponding coseismic displacements.

**Table 3.** Details of SAR data used for coseismic deformation of the 23 January 2022 $M_W$ 5.6 Hala Lake earthquake.

| Satellite | Track | Reference Date | Repeat Date | Perp. B (m) | Inc. Angle | Azi. Angle |
|---|---|---|---|---|---|---|
| Sentinel-1A | T99A | 15 January 2022 | 27 January 2022 | −13.1 | 36.9 | −10.3 |
| Sentinel-1A | T4D | 8 January 2022 | 1 February 2022 | 15.7 | 36.9 | −169.7 |

Notes: Perp. B denotes the perpendicular baseline. Inc. Angle and Azi. Angle represent the incidence and azimuth angles, respectively.

**Table 4.** Details of SAR data used for coseismic deformation of the 25 March 2022 $M_W$ 5.7 Hala Lake earthquake.

| Satellite | Track | Reference Date | Repeat Date | Perp. B (m) | Inc. Angle | Azi. Angle |
|---|---|---|---|---|---|---|
| Sentinel-1A | T99A | 16 March 2022 | 28 March 2022 | −96.6 | 36.9 | −10.3 |
| Sentinel-1A | T4D | 21 March 2022 | 2 April 2022 | 51.2 | 36.9 | −169.7 |

Notes: All the abbreviations in Table 4 are the same as those in Table 3, but for the March 2022 Hala Lake earthquake.

**Table 5.** Details of SAR data used for the total coseismic deformation of the 23 January and 25 March 2022 $M_W$ > 5.5 Hala Lake earthquakes.

| Satellite | Track | Reference Date | Repeat Date | Perp. B (m) | Inc. Angle | Azi. Angle |
|---|---|---|---|---|---|---|
| Sentinel-1A | T99A | 15 January 2022 | 28 March 2022 | −86.9 | 36.9 | −10.3 |
| Sentinel-1A | T4D | 8 January 2022 | 2 April 2022 | 80.2 | 36.9 | −169.7 |

Notes: All the abbreviations in Table 5 are the same as those in Table 3, but for both the 23 January and 25 March 2022 $M_W$ > 5.5 Hala Lake earthquakes.

**Table 6.** Details of SAR data used for postseismic deformation of the 23 January 2022 $M_W$ 5.6 Hala Lake earthquake.

| Satellite | Track | Reference Date | Date Due | No. of Images | Used Interferograms |
|---|---|---|---|---|---|
| Sentinel-1A | T99A | 27 January 2022 | 16 March 2022 | 5 | 10 |
| Sentinel-1A | T4D | 1 February 2022 | 21 March 2022 | 5 | 10 |

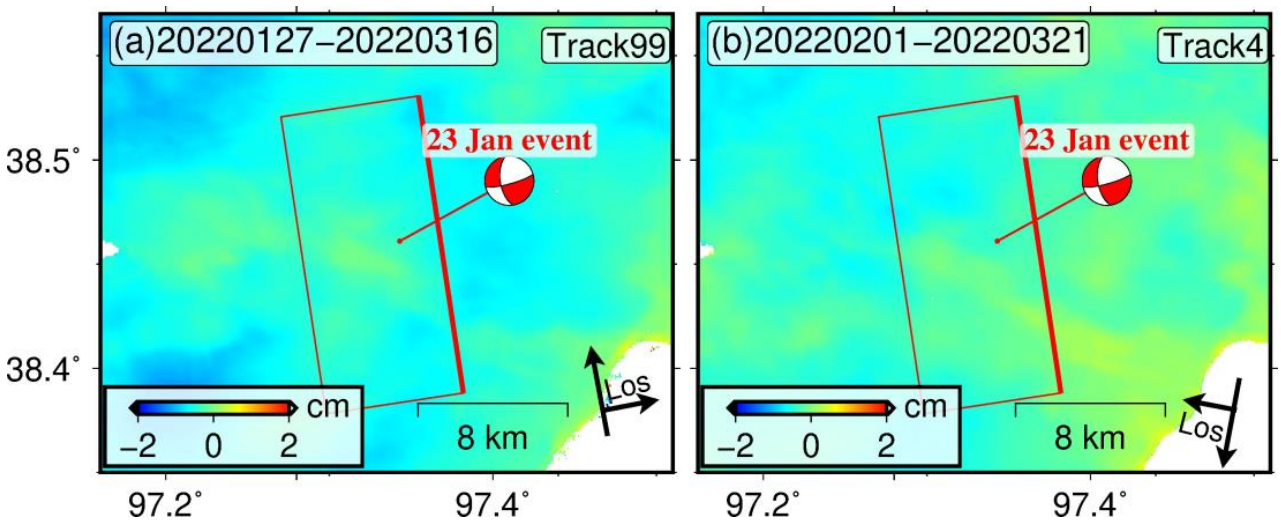


**Figure 3.** (**a**,**b**) are the ascending and descending postseismic cumulative deformation maps of the 23 January 2022 Hala Lake earthquake, respectively. Red rectangular box represents the rupture fault plane from the coseismic slip distribution model of the January 2022 event. The solid red line shows the fault surface trace.

## 4. Geodetic Modelling

To gain an insight into the source characteristics, we exploit the resolution-based resampling method [27] to downsample the coseismic LOS deformation related to the 23 January and 25 March 2022 Menyuan earthquakes (Figure 2i–l) and further invert for slip on the rectangular dislocation, assuming a homogeneous, elastic, and isotropic half-space [28]. At first, we perform a non-linear inversion to hunt for the optimal fault geometrical parameters by means of the multi-peak particle swarm optimization algorithm [29] and then estimate the uncertainty of each obtained fault parameter through Monte Carlo inversions [30] of 100 datasets perturbed with random noise (Figures 4 and 5). Subsequently, we extend the derived fault planes responsible for the two earthquakes along strike and dip directions, respectively, and carry out a linear inversion to resolve the variable slip distribution on the enlarged fault plane subdivided into subpatches of 1 by 1 km. In addition, we added a befitting smoothing factor to the linear inversion by examining the trade-off curve between the RMS and roughness (Figure 6) in order to avoid the abrupt slip variations and further utilize the one-dimensional grid search method to optimize the fault dip during the coseismic slip distribution inversion (Figure 7).

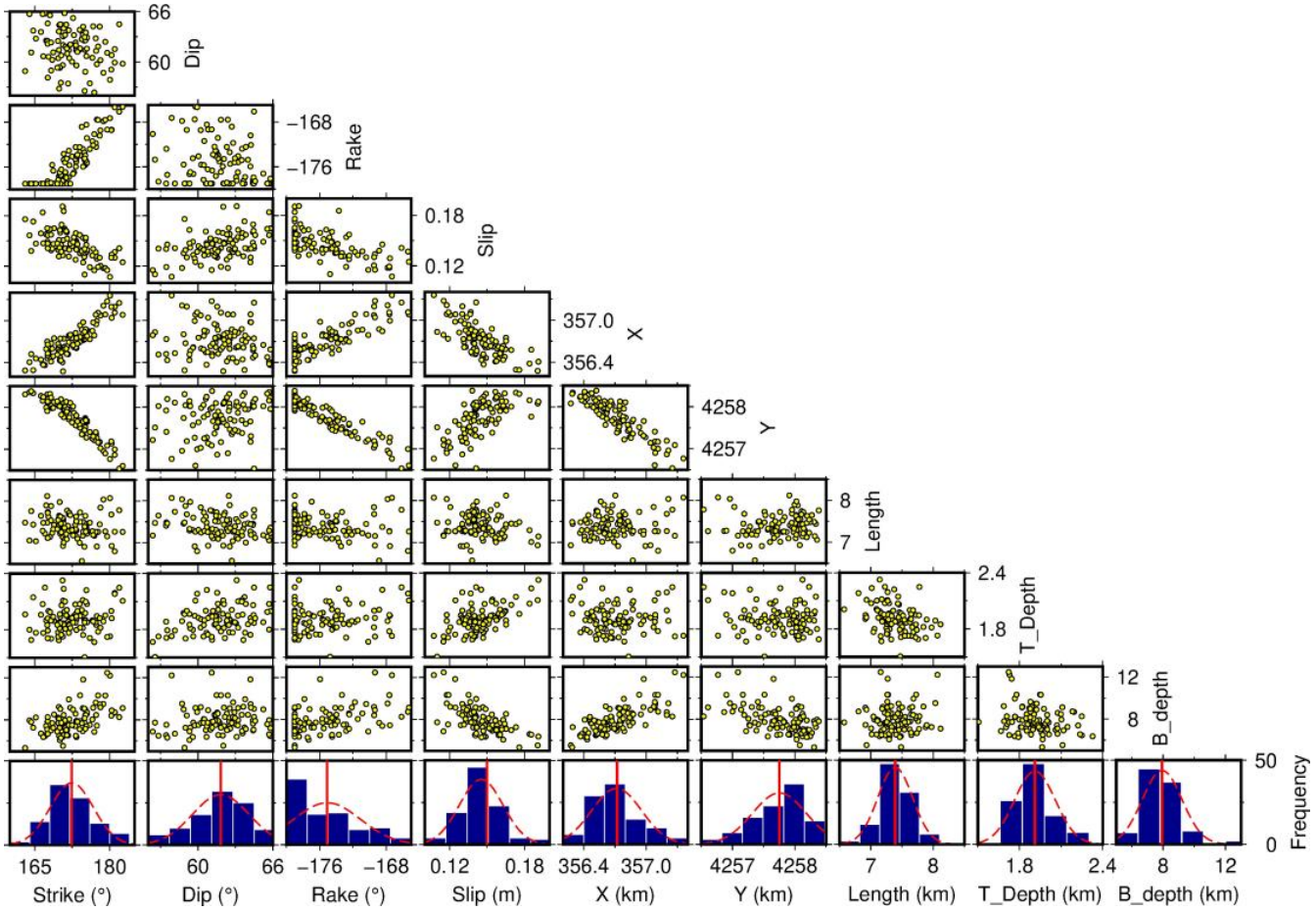


**Figure 4.** Fault geometry parameters for the uniform fault plane of the January 2022 Hala Lake earthquake from the Monte-Carlo analysis. B_depth: the midpoint of the bottom boundary of the uniform fault plane; T_depth: the midpoint of the upper boundary of the uniform fault plane; Histograms show the distribution of the optimal solutions of fault geometry parameters during the 100 inversions. The solid red line represents the optimal value.

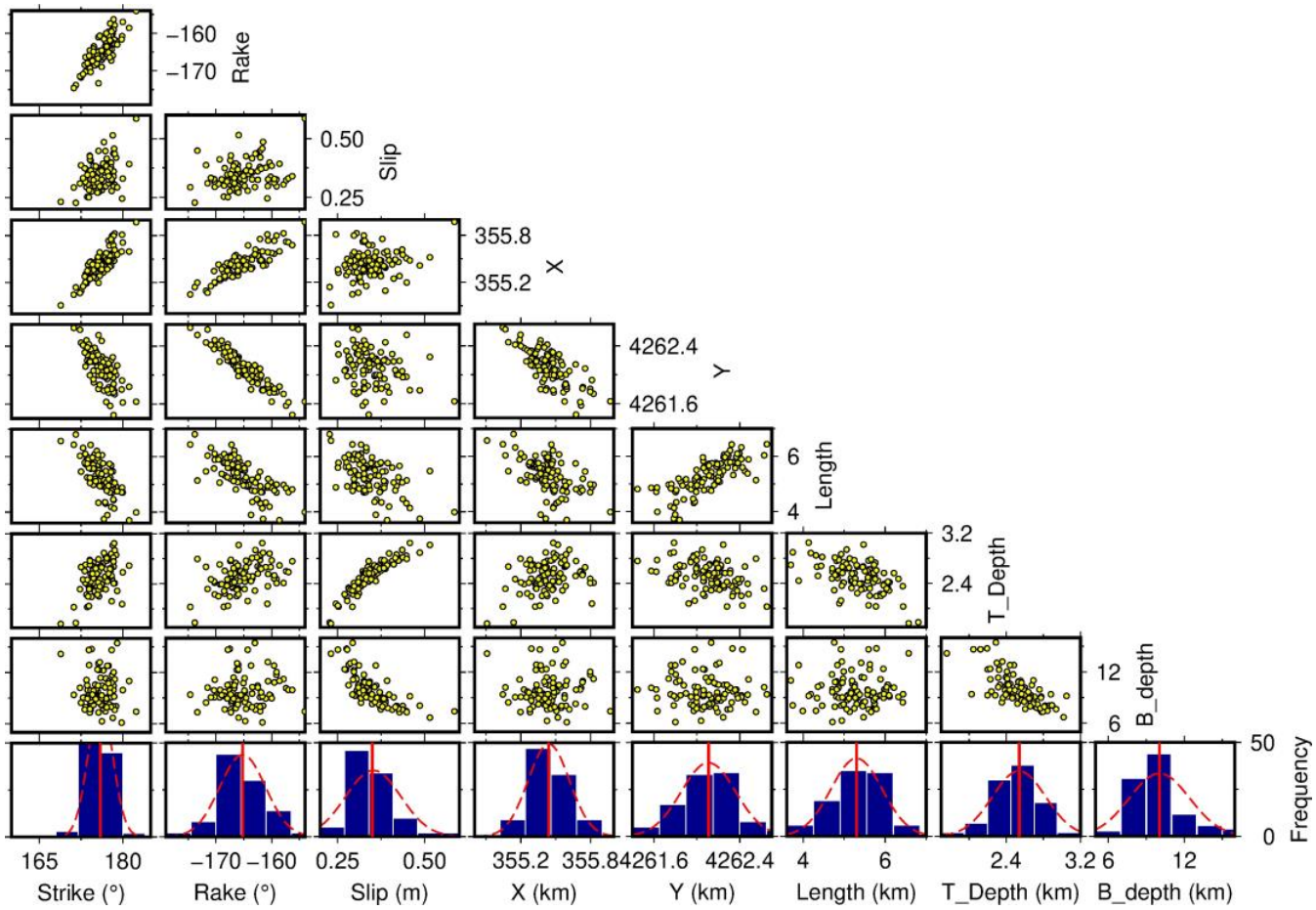


**Figure 5.** All the symbols in Figure 5 are the same as those in Figure 4, but for the uniform fault model of the March 2022 Hala Lake earthquake.

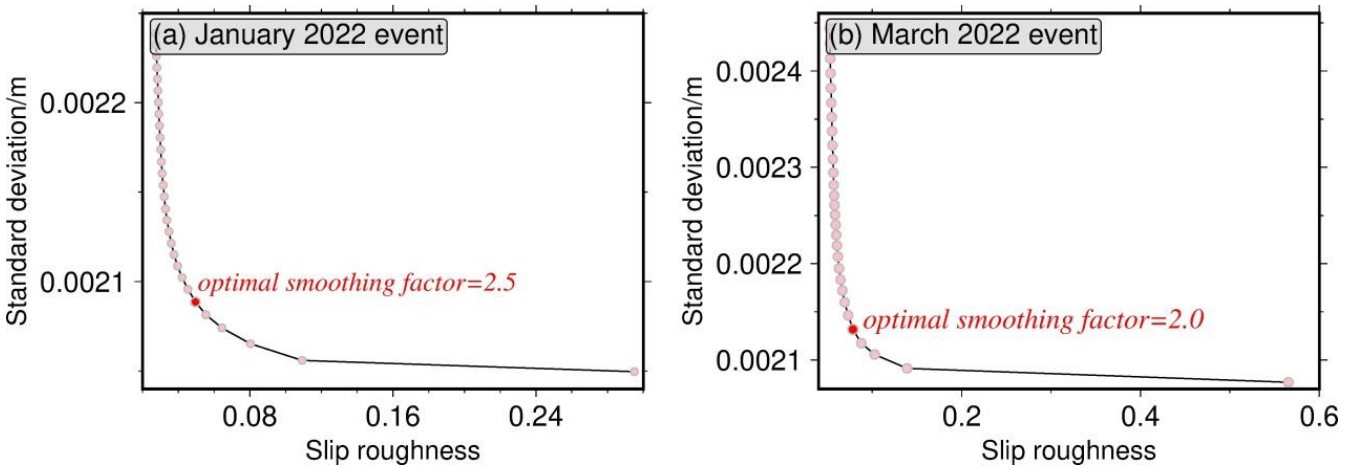


**Figure 6.** Trade-off curve of the standard deviation of data versus the slip roughness. Red circle denotes the selected smoothing factor, which is used to the coseismic slip distribution inversion.

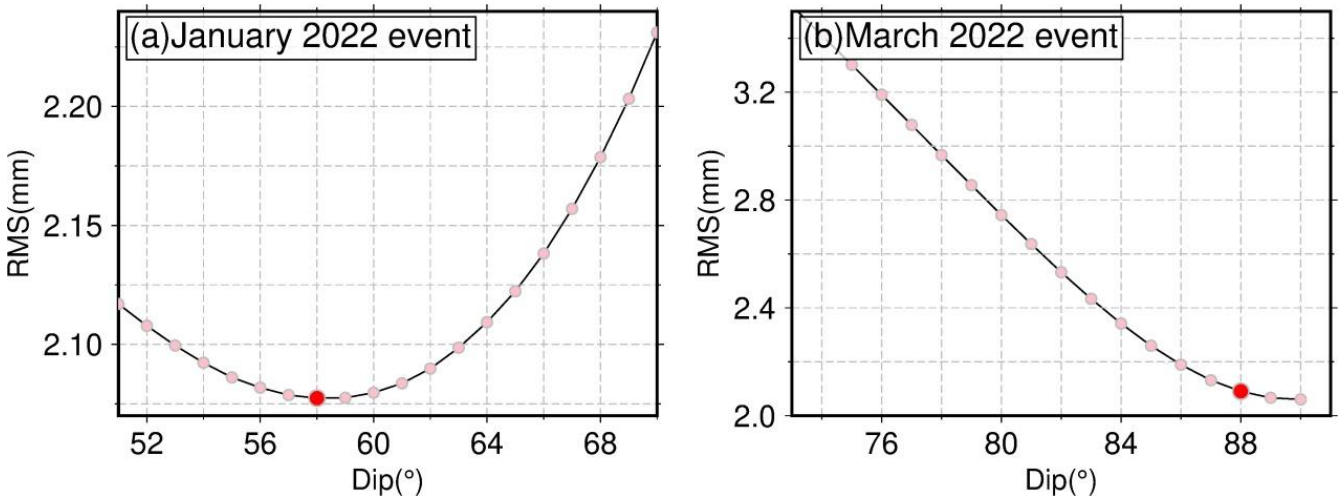


**Figure 7.** Trade-off curve between the RMS and the dip of the rupture fault segment. Red circle indicates the optimal fault dip used in the coseismic slip distribution inversion. In (**b**), the RMS decreases rapidly with increasing dip but no longer decreases significantly when dip reaches 88°, so we regard the 88° as the optimal fault dip.

### *4.1. The 23 January 2022 Hala Lake Earthquake*

According to the detailed analysis of the coseismic interferograms (Figure 2a,b) in Section 2, we believe the west-dipping dextral strike-slip fault to be the causative fault responsible for the January 2022 Hala Lake earthquake and then set a search interval for the fault geometrical parameters. The rake and strike are constrained between −225° and −135°, and 135° and 225°, respectively, while the other fault geometrical parameters are unconstrained. (For example, the search range for the dip is set to 0°~90°). The best-fitting solutions for each fault geometrical parameter shown in Table 1 and Figure 4 reveal an SSE-striking strike-slip fault with a minor normal slip during the Hala Lake earthquake. The uniform coseismic slip of up to ~0.15 m extends from a depth of 7.9 km up to 1.9 km on a ~7.4 km-long and ~6.3 km-wide rupture fault (Table 1 and Figure 4). As a whole, the fault parameters are well-resolved with small uncertainties (Table 1). For example, the fault location (X and Y) has an uncertainty of less than 500 m while the strike, dip, and rake have an uncertainty of less than 4.3°. Moreover, the uniform slip model can reproduce the observed ascending and descending coseismic deformations (Figure 8). The corresponding slip distribution model (Figure 9a–c) shows that the rupture fault is dominated by nearly pure dextral strike-slip faulting, and that most slips are concentrated at a depth from 1.7–7.6 km, with the maximum slip of about 0.21 m at a depth of 3.8 km, suggesting a buried event. The location of the epicenter relative to the inverted slip distribution implies that the coseismic rupture mainly propagates northward unilaterally. The seismic moment generated by the coseismic slip distribution model is ~2.4 × $10^{17}$ Nm, corresponding to $M_W$ 5.6. Compared with the modeled interferograms by the uniform slip model (Figure 8), the detected ascending and descending coseismic deformations can be better explained (Figure 10) with the rms of ~2.5 and 1.4 mm, respectively.

### *4.2. The 25 March 2022 Hala Lake Earthquake*

On the basis of the coseismic interferogram described in Section 2, we consider the seismogenic fault to be a sub-vertical right-lateral strike-slip fault. Initially, we constrain the rake between −225° and −135°, while other source parameters are not restricted. However, after several nonlinear inversions, the dip always reaches its maximum limit of 90°. Hence, we fix the dip to be 87° according to the reported focal mechanism solutions from GCMT (Table 2) and run the inversion again. The optimal uniform slip model (Table 2 and Figure 5) reveals 0.35 m of coseismic slip on a 5.3 km-long and 7.2 km-wide rupture fault and generally fits the observed ascending and descending coseismic deformations (Figure 11).

Furthermore, the fault parameters are well-resolved with small uncertainties (Table 2). For instance, the fault location (X and Y) has an uncertainty of less than 300 m while the strike and rake have an uncertainty of less than 4.1°. The corresponding slip distribution model (Figure 9a,b,d) indicates that the rupture fault is characterized by dextral strike-slip faulting with a slight normal-slip component, and that the majority of the slip is limited at depths between 2.5 and 10 km, with the peak slip of about 0.47 m at a depth of 5.5 km. The location of the epicenter relative to the inverted slip distribution indicates that the coseismic rupture mainly propagates southward unilaterally. Interestingly, the coseismic slip of the March 2022 event terminates just before the junction of the two seismogenic faults responsible for the January and March earthquakes at depths of ~2.5 km (Figure 9e). We suggest that the intersection of the moderate-angle seismogenic fault of the January 2022 event with the high-angle seismogenic fault of the March 2022 event may restrict the slip extent in the March 2022 event to deep depths of <~2.5 km (Figure 9e; e.g., [2]). The seismic moment yielded by the best-fitting slip distribution model is ~4.4 × $10^{17}$ Nm, equal to $M_W$ 5.7. In contrast to the modeled interferograms by the uniform slip model (Figure 11), the best-fitting slip distribution reproduces the observed ascending and descending coseismic deformations better with the rms of ~2.3 and 1.8 mm, respectively (Figure 12).

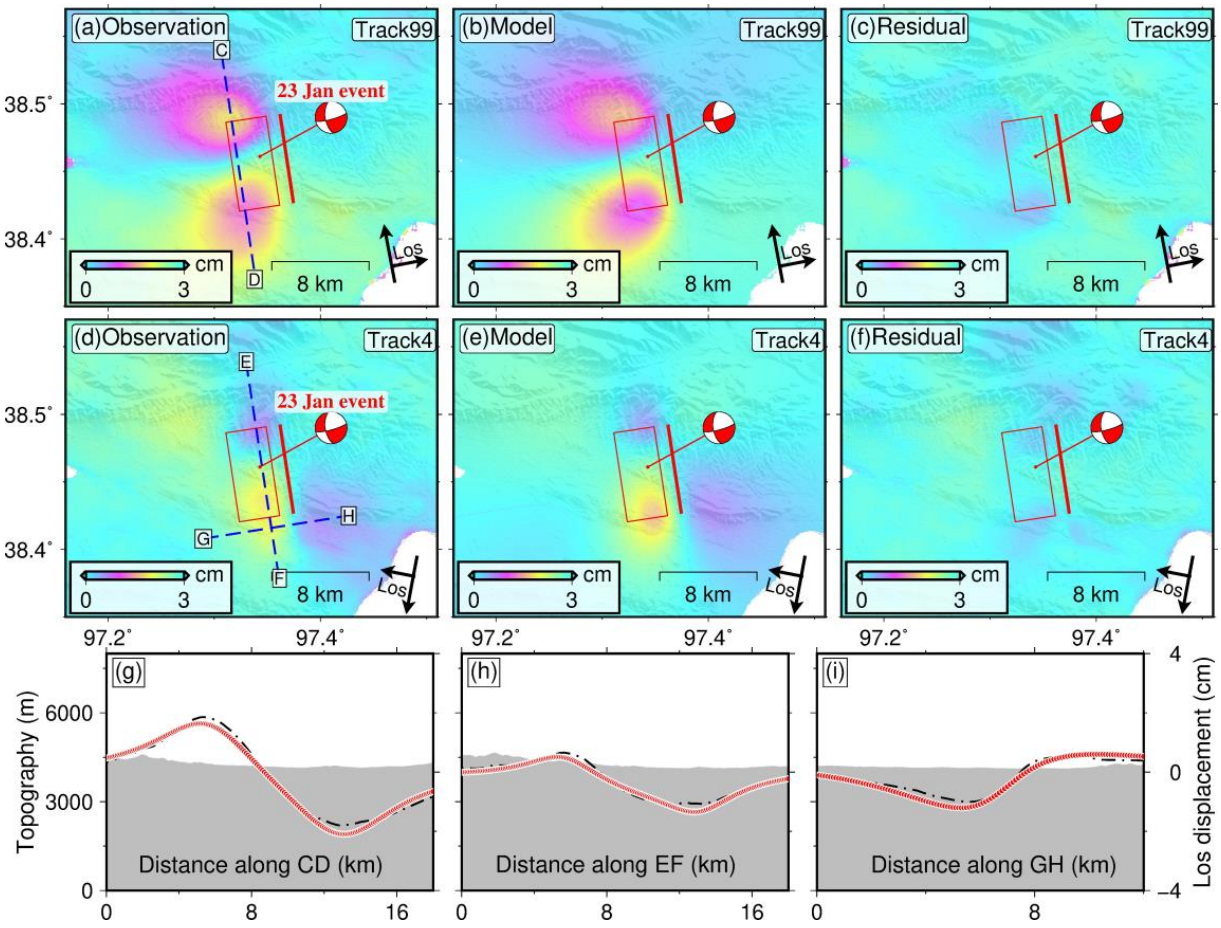


**Figure 8.** (**a**,**d**) are the ascending and descending coseismic interferograms, respectively, covering the 23 January 2022 Hala Lake earthquake. (**b**,**e**) are the modeled interferograms using the uniform slip model of the January 2022 event. (**c**,**f**) are corresponding residuals. The thick red line and thin red box indicate the surface projection of the seismogenic fault and rupture fault plane, respectively, from the uniform slip model of the January 2022 event. (**g**–**i**) are LOS displacements along Profiles CD, EF and GH, respectively. The dashed black line depicts the observed LOS displacement, while the red circles represent the modeled LOS displacement.

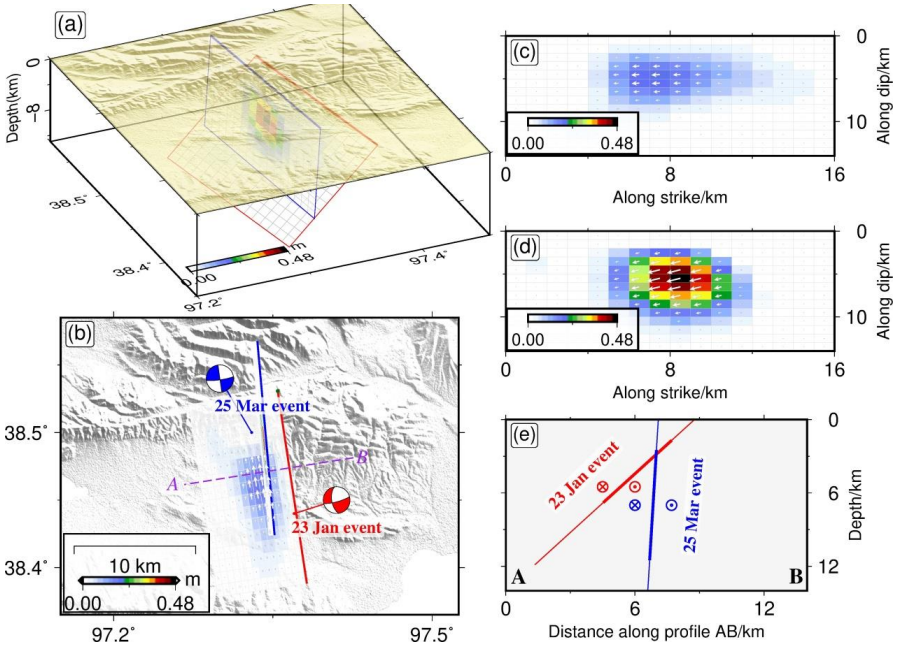


**Figure 9.** (**a**) Three-dimensional view of the coseismic slip distribution models of the January and March 2022 Hala Lake earthquakes. (**b**) Two-dimensional views of the coseismic slip distribution models of the January and March 2022 Hala Lake earthquakes. (**c**,**d**) show coseismic slip distributions of the January and March 2022 Hala Lake events along the strike and dip directions, respectively. (**e**) Fault substructures along the profile AB. Thin red and blue lines indicate the rupture fault planes of the two Hala Lake events, respectively, and the thick red and blue lines denote the major slip area.

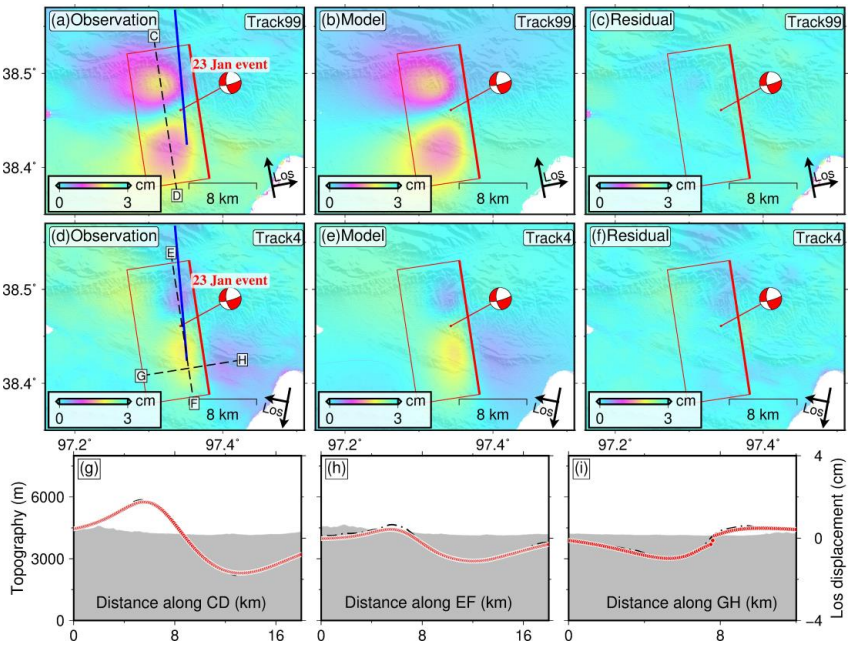


**Figure 10.** (**a**,**d**) are the ascending and descending coseismic interferograms, respectively, covering the 23 January 2022 Hala Lake earthquake. (**b**,**e**) are the modeled interferograms using the coseismic slip distribution models of the January 2022 event. (**c**,**f**) are corresponding residuals. The thick red line and thin red box indicate the surface projection of the seismogenic fault and rupture fault plane, respectively, from the coseismic slip distribution model of the January 2022 event. (**g**–**i**) are LOS displacements along Profiles CD, EF and GH, respectively. The dashed black line depicts the observed LOS displacement, while the red circles represent the modeled LOS displacement.

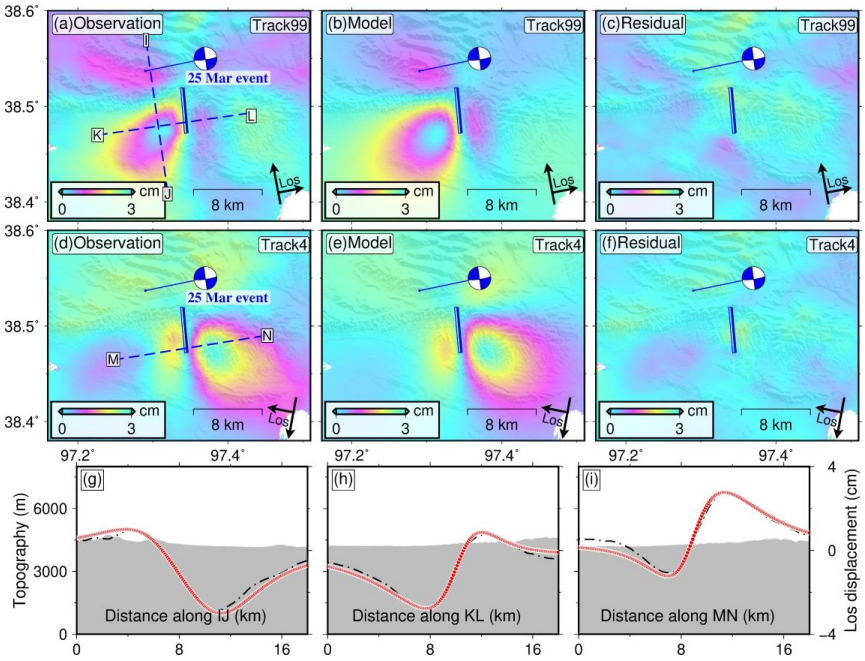


**Figure 11.** (**a**,**d**) are ascending and descending coseismic interferograms, respectively, covering the 25 March 2022 Hala Lake earthquake. (**b**,**e**) are modeled interferograms using the uniform slip model of the March 2022 event. (**c**,**f**) are corresponding residuals. The thick blue line and thin blue box indicate the surface projection of seismogenic fault and rupture fault plane, respectively, from the uniform slip model of the March 2022 event. (**g**–**i**) are LOS displacements along the profile IJ, KL and MN, respectively. The dashed black line depicts the observed LOS displacement, while the red circles represent the modeled LOS displacement.

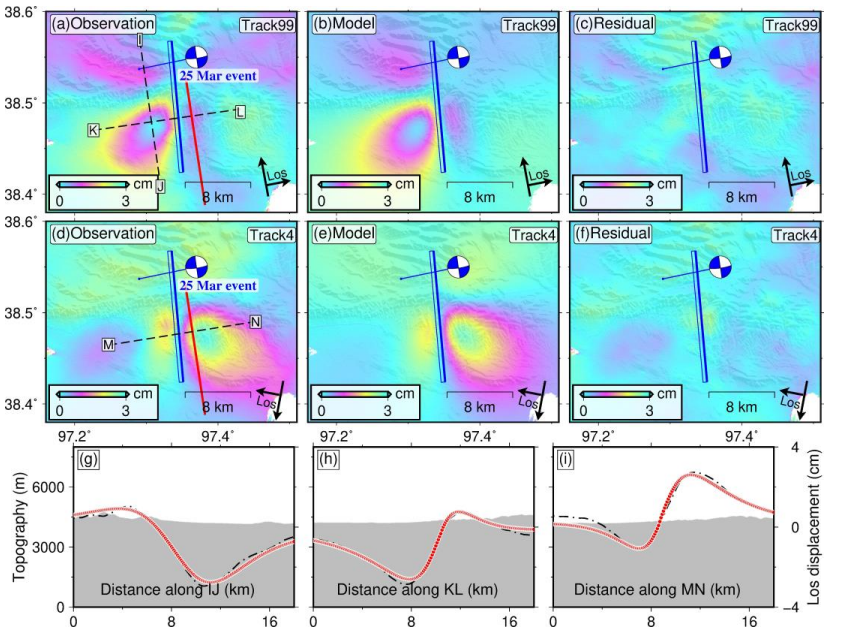


**Figure 12.** (**a**,**d**) are ascending and descending coseismic interferograms, respectively, covering the 25 March 2022 Hala Lake earthquake. (**b**,**e**) are modeled interferograms using the coseismic slip distribution model of the March 2022 event. (**c**,**f**) are corresponding residuals. The thick blue line and thin blue box indicate the surface projection of seismogenic fault and rupture fault plane, respectively, from the coseismic slip distribution model of the March 2022 event. (**g**–**i**) are LOS displacements along the profile IJ, KL and MN, respectively. The dashed black line depicts the observed LOS displacement, while the red circles represent the modeled LOS displacement.

## 5. Discussion

### *5.1. Relationship between the 7 January 2022 $M_W$ 6.7 Menyuan Earthquake and the January and March 2022 $M_W$ > 5.5 Hala Lake Earthquakes*

A coseismic slip during a large earthquake can change the stress status of the nearby faults, thus resulting in the advance or delay of the future seismic events [31–33]. Considering that the 7 January 2022 $M_W$ 6.7 Menyuan earthquake occurred ~350 km southeast of the two Hala Lake earthquakes and only 16 days before the first Hala Lake event (Figure 1a), we utilize the coulomb failure stress (CFS) Formula (1) [34] to calculate the coseismic CFS changes due to the 2022 Menyuan event at the maximum slip area of the two Hala Lake events with a common friction coefficient of 0.4 (e.g., [33]).

$$CFS = \Delta\tau - \mu'\Delta\sigma \quad (1)$$

Thereinto, $\mu'$ represents the effective friction coefficient, whereas $\Delta\tau$ and $\Delta\sigma$ indicate the shear stress and normal stress changes, respectively [34].

Furthermore, it should be noted that the positive stress value usually encourages a rupture, while a negative one often prohibits a rupture. The previously published coseismic slip distribution model of the 2022 Menyuan earthquake, which can be openly obtained from the Zenodo (https://zenodo.org/record/6816540#.YsuwwciVVbl, accessed on 1 January 2023), is exploited as the source model, while the focal mechanism solutions of the two Hala Lake events (Tables 1 and 2) are regarded as the receiver mechanism. Finally, the open psgrn/pscmp program [35] is used to carry out the stress perturbation calculations. The derived CFS results (Figure 13) show a negligible stress change of ~0 Bar on the rupture area of the two Hala Lake earthquakes, implying that the occurrence of the 2022 Menyuan earthquake had a limited effect on promoting the occurrence of the two Hala Lake events.

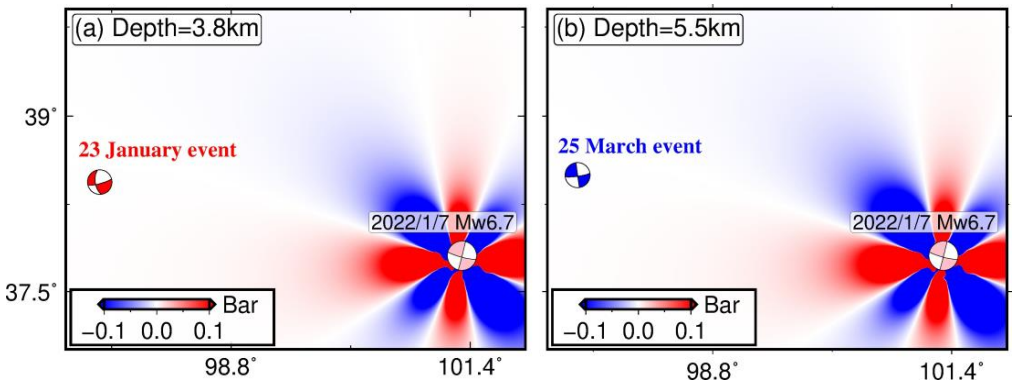


**Figure 13.** (**a**) Coseismic CFS changes at a depth of 3.8 km induced by the 2022 Menyuan earthquake. The focal mechanism solutions of the 23 January 2022 Hala Lake earthquake (Table 1) are set as the receiver mechanism. The depth of 3.8 km, where the maximum slip is located, is set as the calculated depth. (**b**) Coseismic CFS changes at a depth of 5.5 km induced by the 2022 Menyuan earthquake. The focal mechanism solutions of the 25 March 2022 Hala Lake earthquake (Table 2) are set as the receiver mechanism. The depth of 5.5 km, where the maximum slip occurs, is chosen as the calculated depth.

### *5.2. Possible Causes for The Stop-Start Rupture of the Two Hala Lake Events*

Geometric complexities consisting of fault segmentation, intersection, stepovers, and bends are thought as a barrier to rupture propagation, thus halting an instantaneous multi-fault rupture in one large earthquake (e.g., [1,36]). Our preliminary geodetic observation reveals a complex two-fault delayed failure during the two 2022 Hala Lake earthquakes that span a long period of about two months. Further InSAR modeling shows that, although the strike (a difference of ~4°) and location (a difference of ~2 km) of the two seismogenic faults are basically the same, their dip angles exhibit a quite difference (~30°) from each other (Figures 7 and 9b). This significant discrepancy in fault geometry implies an obvious fault segmentation that is capable of stopping the rupture propagation from one fault segment

to another (e.g., [37]). For example, the 2018 Lombok earthquake sequence is considered as a failed multi-segment large earthquake mainly because the distinct dip and strike differences in fault geometry control the rupture termination in each event [38]. Similarly, we highlight that the prominent fault dip difference between the two Hala Lake events may prevent two simultaneous ruptures in a single large earthquake. The static stress transfer is generally known as the major cause for the rupture reinitiation of an earthquake doublet or seismic sequence (e.g., [39–41]). To assess this hypothesis, we quantify the effect of the coseismic coulomb failure stress (CFS) changes induced by the January 2022 Hala Lake earthquake (source fault) on the March 2022 Hala Lake earthquake (receiver fault) with a common friction coefficient of 0.4 (e.g., [33]). Our result (Figure 14) reveals a negative stress value of up to ~−1.1 bar at the main slip area of the March 2022 Hala Lake event, which does not support the hypothesis that coseismic CFS played a crucial role in promoting the rupture reinitiation of the later Hala Lake earthquake. As another triggering mechanism, the afterslip propagation may be an important cause for promoting the restart of the slip of the later earthquake because the cumulative CFS due to postseismic afterslips may further encourage failure [1,2,42]. However, we find that no significant postseismic signals are detected during the period from 23 January to 25 March 2022 (Figure 3), indicating a limited afterslip magnitude. In addition, fluid migration following the large earthquake is also considered to be capable of encouraging rupture reinitiation since the arrival of the underground fluids are able to increase pore-pressure and thus unclamp the critically stressed fault to allow its movement [43]. We suggest that a detailed mapped subsurface fault networks in the epicentral area needs to be investigated for analyzing the channel of fluid diffusion, thus verifying the role of fluid migration in the two 2022 Hala Lake earthquakes (e.g., [2]). In particular, the roughly two months' delay between the two Hala Lake events may be also determined by the fluid migration, which will need to be verified in the future investigation by collecting relocated aftershock data (e.g., [2]).

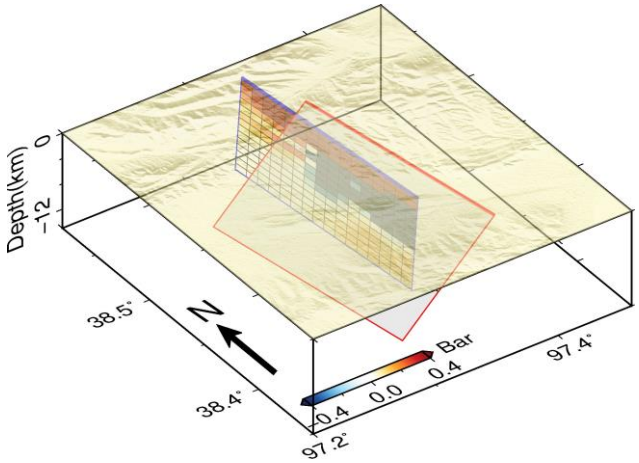


**Figure 14.** Coseismic CFS changes along the rupture fault of the 25 March 2022 Hala Lake earthquake induced by the 23 January 2022 Hala Lake earthquake. Red and blue rectangular frames are the rupture fault planes from the coseismic slip distribution model of the January and March 2022 events, respectively.

### *5.3. Regional Seismic Hazards Assessment*

As the two largest earthquakes around Hala Lake since the 15 March 1927 $M_w$ 6.2 earthquake (Figure 1c), the 2022 $M_w$ 5.6 and $M_w$ 5.7 Hala Lake earthquakes, which ruptured closely in space, make more sense in the aspect of assessing the regional seismic risk. In order to investigate the effect of the two Hala Lake earthquakes on the regional seismicity, we calculated the static CFS changes at the depth of 10 km where the most aftershocks are located. The result (Figure 15a,b) reveals that ~58% of aftershocks are concentrated in the regions of positive CFS of >0.1 Bar (an earthquake triggering threshold [44]), indicating that the statics CFS is not the unique triggering mechanism for

aftershocks. However, it is worth noting that only $M_S > 3.0$ aftershocks have been collected and that the aftershock distribution is not the result of relocated aftershock sequences, which requires further research on the trigger mechanisms of aftershocks. To explore the impact of the two events on the surrounding faults, we utilize coseismic slip distributions of these two earthquakes (source fault) to calculate the CFS changes along the mapped faults (receiver fault). According to the known surface trace, a strike-variable fault plane composed of many discrete sub-patches with a size of 2 km by 2 km, is constructed with the purpose to obtain detailed stress distribution along the entire subsurface fault structure e.g., [8]. In detail, we first divide the mapped fault traces into small segments of a fixed length of 2 km along the strike direction and then extend the width of the fault plane to 16 km along the down-dip direction by applying a constant value of dip e.g., [45]. Moreover, we set a pure dip-slip mechanism (a rake of 90°) for the known DHLTF, DHNSF and DXS-SLF with a constant dip of 45° and a pure dextral strike-slip mechanism (a rake of 180°) for the mapped ELSF with a steep dip of 90° as the receiver mechanism. The acquired total CFS changes (Figure 15e) due to the 23 January and 25 March 2022 Hala Lake earthquakes (Figure 15c,d) exhibiting stress unloading on the eastern segment of the DHLTF and DHNSF (a stress value of up to ~−0.03 bar and −0.014 bar, respectively), the western segment of the DXS-SLF (maximum ~−0.044 bar), and the southern segment of the ELSF (up to ~−0.025 bar). In addition, given that the eastern segment of the DXS-SLF and the northern segment of the ELSF reveal stress loading (Figure 15e), we should pay more attention to these fault segments.

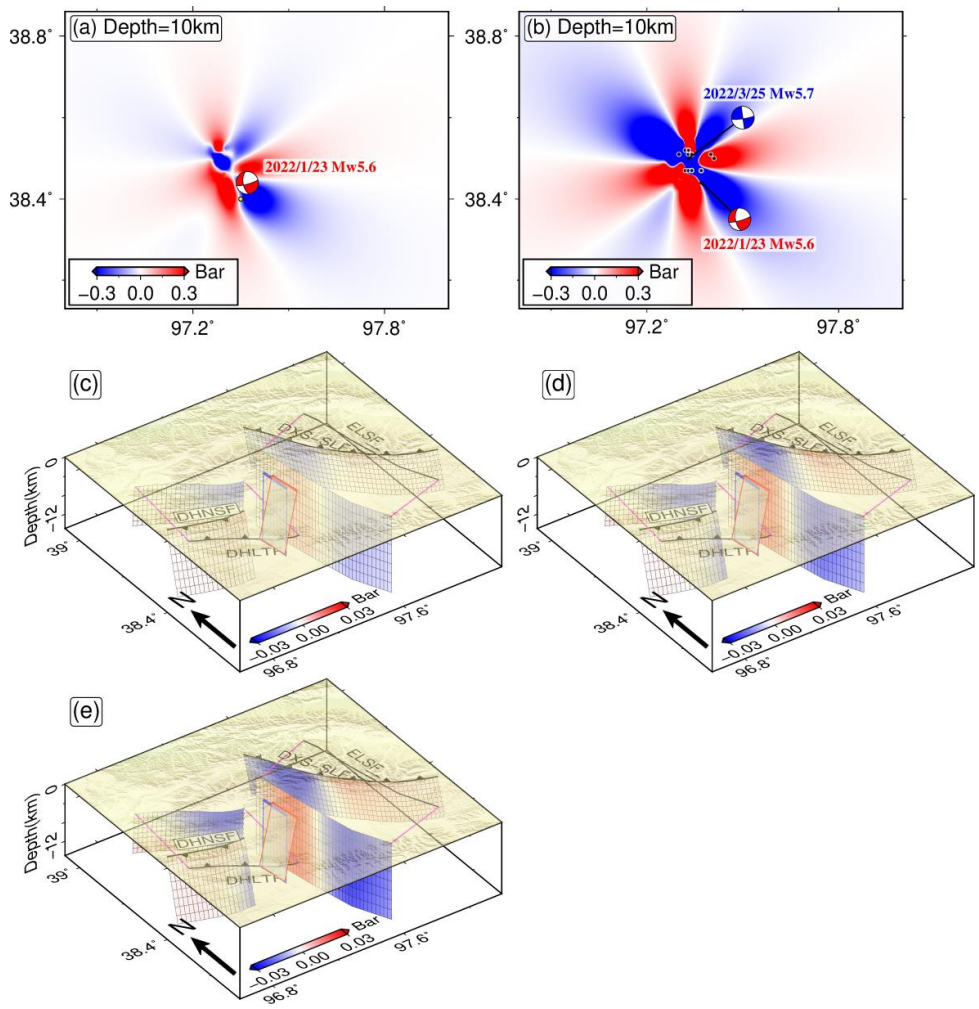


**Figure 15.** (**a**) Coseismic CFS changes induced by the 23 January 2022 $M_W$ 5.6 Hala Lake earthquake

at a depth of 10 km. The focal mechanism solutions (Table 1) of the January event are set as the receiver mechanism. (**b**) Coseismic CFS changes caused by the 23 January and 25 March 2022 $M_W$ > 5.5 Hala Lake earthquakes at a depth of 10 km. The focal mechanism solutions (Table 2) of the March event are regarded as the receiver mechanism. (**c**) Coseismic CFS changes along the known DHLTF, DHNSF, ELSF and DXS-SLF induced by the January 2022 Hala Lake event. (**d**) Coseismic CFS changes along the known DHLTF, DHNSF, ELSF and DXS-SLF due to the March 2022 Hala Lake event. (**e**) Coseismic CFS changes along the known DHLTF, DHNSF, ELSF, and DXS-SLF caused by both the January and March 2022 Hala Lake events. The red and blue rectangular boxes represent the rupture fault planes from the coseismic slip distribution models of the January and March 2022 Hala Lake events, respectively. The magenta lines in Figure (**c**–**e**) show where the fault planes have moved.

## 6. Conclusions

We investigate the coseismic rupture behaviors of the January and March 2022 Hala Lake earthquakes on the basis of the coseismic InSAR observations. The two Hala Lake events ruptured two unmapped west-dipping, left-stepping dextral strike-slip faults with a dip of 58° and 88°, respectively. Most of the slip of the January event is confined to depths from 1.7–7.6 km with the maximum slip of ~0.21 m at a depth of 3.8 km while the majority of slip of the March event is limited at depths between 2.5 and 10 km, with the peak slip of ~0.47 m at a depth of 5.5 km. According to the in-depth analysis of the possible causes for the stop-start rupture of the two Hala Lake earthquakes, we propose that fault segmentation plays a key role in impeding the rupture propagation, thus resulting in a two-fault delayed rupture, and that fluid migration may promote the slip reinitiation of the later Hala Lake event, which requires further analysis. Additionally, we should note the eastern segment of the DXS-SLF and the northern segment of the ELSF due to the state of stress loading.

**Author Contributions:** Conceptualization, J.Y. and C.X.; methodology, J.Y.; software, J.Y.; validation, J.Y., C.X. and Y.W.; formal analysis, J.Y.; investigation, J.Y.; resources, J.Y.; data curation, J.Y.; writing—original draft preparation, J.Y. and C.X.; writing—review and editing, J.Y., C.X. and Y.W; visualization, J.Y.; supervision, C.X.; project administration, C.X.; funding acquisition, C.X. All authors have read and agreed to the published version of the manuscript.

**Funding:** This research was funded by the National Natural Science Foundation of China (Nos. 42074007, 41721003, 42130101 and 41974004).

**Data Availability Statement:** The original Sentinel-1 images are downloaded from the European Space Agency (https://scihub.copernicus.eu/dhus/#/home, accessed on 1 January 2023). The coseismic slip distribution model of the 7 January 2022 $M_W$ 6.7 Menyuan earthquake is openly available from Zenodo (https://zenodo.org/record/6816540#.YsuwwciVVbl, accessed on 1 January 2023).

**Conflicts of Interest:** The authors declare no conflict of interest.

## References

1. Yang, J.; Xu, C.; Wen, Y.; Xu, G. Complex coseismic and postseismic faulting during the 2021 northern Thessaly (Greece) earthquake sequence illuminated by InSAR observations. *Geophys. Res. Lett.* **2022**, *49*, e2022GL098545. [CrossRef]
2. Walters, R.J.; Gregory, L.C.; Wedmore, L.N.; Craig, T.J.; McCaffrey, K.; Wilkinson, M.; Chen, J.; Li, Z.; Elliott, J.R.; Goodall, H.; et al. Dual control of fault intersections on stop-start rupture in the 2016 Central Italy seismic sequence. *Earth Planet. Sci. Lett.* **2018**, *500*, 1–14. [CrossRef]
3. Elliott, J.R.; Walters, R.J.; Wright, T.J. The role of space-based observation in understanding and responding to active tectonics and earthquakes. *Nat. Commun.* **2016**, *7*, 13844. [CrossRef]
4. Massonnet, D.; Rossi, M.; Carmona, C.; Adragna, F.; Peltzer, G.; Feigl, K.; Rabaute, T. The displacement field of the Landers earthquake mapped by radar interferometry. *Nature* **1993**, *364*, 138–142. [CrossRef]
5. Cakir, Z.; Akoglu, A.M. Synthetic aperture radar interferometry observations of the *M* = 6.0 Orta earthquake of 6 June 2000 (NW Turkey): Reactivation of a listric fault. *Geochem. Geophys. Geosyst.* **2008**, *9*, Q08009. [CrossRef]
6. Yang, J.; Xu, C.; Wang, S.; Wang, X. Sentinel-1 observation of 2019 Mw 5.7 Acıpayam earthquake: A blind normal-faulting event in the Acipayam basin, southwestern Turkey. *J. Geodyn.* **2020**, *135*, 101707. [CrossRef]

7. Yang, J.; Xu, C.; Wen, Y. The 2019 Mw 5.9 Torkaman chay earthquake in Bozgush mountain, NW Iran: A buried strike-slip event related to the sinistral Shalgun-Yelimsi fault revealed by InSAR. *J. Geodyn.* **2020**, *141*, 101798. [CrossRef]
8. Yang, J.; Xu, C.; Wen, Y.; Xu, G. The July 2020 M w 6.3 Nima Earthquake, Central Tibet: A Shallow Normal-Faulting Event Rupturing in a Stepover Zone. *Seismol. Res. Lett.* **2022**, *93*, 45–55. [CrossRef]
9. Xu, X.W.; Tan, X.B.; Yu, G.H.; Wu, G.D.; Fang, W.; Chen, J.B.; Song, H.P.; Shen, J. Normal-and oblique-slip of the 2008 Yutian earthquake: Evidence for eastward block motion, northern Tibetan Plateau. *Tectonophysics* **2013**, *584*, 152–165. [CrossRef]
10. Yuan, D.Y.; Champagnac, J.D.; Ge, W.P.; Molnar, P.; Zhang, P.Z.; Zheng, W.J.; Zhang, H.P.; Liu, X.W. Late Quaternary right-lateral slip rates of faults adjacent to the lake Qinghai, northeastern margin of the Tibetan Plateau. *Bulletin* **2011**, *123*, 2016–2030. [CrossRef]
11. Zheng, W.J.; Zhang, P.Z.; He, W.G.; Yuan, D.Y.; Shao, Y.X.; Zheng, D.W.; Ge, W.P.; Wei, M. Transformation of displacement between strike-slip and crustal shortening in the northern margin of the Tibetan Plateau: Evidence from decadal GPS measurements and late Quaternary slip rates on faults. *Tectonophysics* **2013**, *584*, 267–280. [CrossRef]
12. Jian, H.Z.; Wang, L.F.; Ren, Z.K.; Gong, W.Y.; LI, Y.C.; LIU, J.R. Present-day slip rate and interseismic fault coupling along the Elashan fault using GPS. *Chin. J. Geophys.* **2020**, *63*, 1127–1142.
13. Pan, Z.; Yun, Z.; Shao, Z. Contemporary crustal deformation of Northeast Tibet from geodetic investigations and a comparison between the seismic and geodetic moment release rates. *Phys. Earth Planet. Inter.* **2020**, *304*, 106489. [CrossRef]
14. Wen, Y.; Li, Z.; Xu, C.; Ryder, I.; Bürgmann, R. Postseismic motion after the 2001 MW 7.8 Kokoxili earthquake in Tibet observed by InSAR time series. *J. Geophys. Res. Solid Earth* **2012**, *117*, B08405. [CrossRef]
15. Li, Y.; Jiang, W.; Li, Y.; Shen, W.; He, Z.; Li, B.; Li, Q.; Jiao, Q.; Tian, Y. Coseismic Rupture Model and Tectonic Implications of the January 7 2022, Menyuan Mw 6.6 Earthquake Constraints from InSAR Observations and Field Investigation. *Remote Sens.* **2022**, *14*, 2111. [CrossRef]
16. Gan, C.; Ming, A.; Wenjun, Z.; Haiyun, B.; Jinrui, L.; Yipeng, Z.; Weipeng, G.; Dongli, Z.; Rong, H. Nonrigid Bookshelf Kinematics of Northeastern Tibet: Constrains from Fault Slip Rates around the Qinghai Lake and Chaka-Gonghe Basins. *Lithosphere* **2021**, *2021*, 4115729. [CrossRef]
17. Cheng, F.; Zuza, A.V.; Haproff, P.J.; Wu, C.; Neudorf, C.; Chang, H.; Li, X.; Li, B. Accommodation of India–Asia convergence via strike-slip faulting and block rotation in the Qilian Shan fold–thrust belt, northern margin of the Tibetan Plateau. *J. Geol. Soc.* **2021**, *178*, jgs2020-20. [CrossRef]
18. Werner, C.; Wegmüller, U.; Strozzi, T.; Wiesmann, A. Gamma SAR and interferometric processing software. In Proceedings of the ERS-ENVISAT Symposium, Gothenburg, Sweden, 16–20 October 2000; Volume 1620, p. 1620.
19. Wegnüller, U.; Werner, C.; Strozzi, T.; Wiesmann, A.; Frey, O.; Santoro, M. Sentinel-1 support in the GAMMA software. *Procedia Comput. Sci.* **2016**, *100*, 1305–1312. [CrossRef]
20. Goldstein, R.M.; Werner, C.L. Radar interferogram filtering for geophysical applications. *Geophys. Res. Lett.* **1998**, *25*, 4035–4038. [CrossRef]
21. Goldstein, R.M.; Zebker, H.A.; Werner, C.L. Satellite radar interferometry: Two-dimensional phase unwrapping. *Radio Sci.* **1998**, *23*, 713–720. [CrossRef]
22. Cavalié, O.; Doin, M.P.; Lasserre, C.; Briole, P. Ground motion measurement in the Lake Mead area, Nevada, by differential synthetic aperture radar interferometry time series analysis: Probing the lithosphere rheological structure. *J. Geophys. Res. Solid Earth* **2007**, *112*, B03403. [CrossRef]
23. Funning, G.J.; Parsons, B.; Wright, T.J.; Jackson, J.A.; Fielding, E.J. Surface displacements and source parameters of the 2003 Bam (Iran) earthquake from Envisat advanced synthetic aperture radar imagery. *J. Geophys. Res. Solid Earth* **2005**, *110*, B09406. [CrossRef]
24. Zhang, Y.; Fattahi, H.; Amelung, F. Small baseline InSAR time series analysis: Unwrapping error correction and noise reduction. *Comput. Geosci.* **2019**, *133*, 104331.
25. Fattahi, H.; Amelung, F. DEM error correction in InSAR time series. *IEEE Trans. Geosci. Rem. Sens.* **2013**, *51*, 4249–4259. [CrossRef]
26. Fattahi, H.; Amelung, F. InSAR observations of strain accumulation and fault creep along the Chaman Fault system, Pakistan and Afghanistan. *Geophys. Res. Lett.* **2016**, *43*, 8399–8406. [CrossRef]
27. Lohman, R.B.; Simons, M. Some thoughts on the use of InSAR data to constrain models of surface deformation: Noise structure and data downsampling. *Geochem. Geophys. Geosystems* **2005**, *6*, Q01007. [CrossRef]
28. Okada, Y. Surface deformation due to shear and tensile faults in a half-space. *Bull. Seismol. Soc. Am.* **1985**, *75*, 1135–1154. [CrossRef]
29. Feng, W.; Li, Z.; Elliott, J.R.; Fukushima, Y.; Hoey, T.; Singleton, A.; Cook, R.; Xu, Z.H. The 2011 MW 6.8 Burma earthquake: Fault constraints provided by multiple SAR techniques. *Geophys. J. Int.* **2013**, *195*, 650–660. [CrossRef]
30. Parsons, B.; Wright, T.; Rowe, P.; Andrews, J.; Jackson, J.; Walker, R.; Khatib, M.; Tablebian, M.; Bergman, E.; Engdahl, E.R. The 1994 Sefidabeh (eastern Iran) earthquakes revisited: New evidence from satellite radar interferometry and carbonate dating about the growth of an active fold above a blind thrust fault. *Geophys. J. Int.* **2006**, *164*, 202–217. [CrossRef]
31. Symithe, S.J.; Calais, E.; Haase, J.S.; Freed, A.M.; Douilly, R. Coseismic slip distribution of the 2010 M 7.0 Haiti earthquake and resulting stress changes on regional faults. *Bull. Seismol. Soc. Am.* **2013**, *103*, 2326–2343. [CrossRef]
32. Parsons, T.; Stein, R.S.; Simpson, R.W. Stress sensitivity of fault seismicity: A comparison between limited-offset oblique and major strike-slip faults. *J. Geophys. Res. Solid Earth* **1999**, *104*, 20183–20202. [CrossRef]
33. Freed, A.M. Earthquake triggering by static, dynamic, and postseismic stress transfer. *Annu. Rev. Earth Planet. Sci.* **2005**, *33*, 335–367. [CrossRef]

34. Stein, R.S.; King, G.C.; Lin, J. Change in failure stress on the southern San Andreas fault system caused by the 1992 magnitude = 7.4 Landers earthquake. *Science* **1992**, *258*, 1328–1332. [CrossRef]
35. Wang, R.; Lorenzo-Martin, F.; Roth, F. PSGRN/PSCMP—A new code for calculating co-and post-seismic deformation, geoid and gravity changes based on the viscoelastic-gravitational dislocation theory. *Comput. Geosci.* **2006**, *32*, 527–541. [CrossRef]
36. Biasi, G.P.; Wesnousky, S.G. Steps and gaps in ground ruptures: Empirical bounds on rupture propagation. *Bull. Seismol. Soc. Am.* **2016**, *106*, 1110–1124. [CrossRef]
37. Zhang, P.; Slemmons, D.B.; Mao, F. Geometric pattern, rupture termination and fault segmentation of the Dixie Valley-Pleasant Valley active normal fault system, Nevada, USA. *J. Struct. Geol.* **1991**, *13*, 165–176. [CrossRef]
38. Wang, C.; Wang, X.; Xiu, W.; Zhang, B.; Zhang, G.; Liu, P. Characteristics of the seismogenic faults in the 2018 Lombok, Indonesia, earthquake sequence as revealed by inversion of InSAR measurements. *Seismol. Res. Lett.* **2020**, *91*, 733–744. [CrossRef]
39. Hubert, A.; King, G.; Armijo, R.; Meyer, B.; Papanastasiou, D. Fault re-activation, stress interaction and rupture propagation of the 1981 Corinth earthquake sequence. *Earth Planet. Sci. Lett.* **1996**, *142*, 573–585. [CrossRef]
40. King, G.C.P.; Cocco, M. Fault interaction by elastic stress changes: New clues from earthquake sequences. *Adv. Geophys.* **2001**, *44*, 1–38.
41. Kroll, K.A.; Richards-Dinger, K.B.; Dieterich, J.H.; Cochran, E.S. Delayed seismicity rate changes controlled by static stress transfer. *J. Geophys. Res. Solid Earth* **2017**, *122*, 7951–7965. [CrossRef]
42. Salman, R.; Lindsey, E.O.; Lythgoe, K.H.; Bradley, K.; Muzli, M.; Yun, S.H.; Chin, S.T.; Tay, C.J.; Costa, F.; Wei, S.J.; et al. Cascading partial rupture of the Flores thrust during the 2018 Lombok earthquake sequence, Indonesia. *Seismol. Res. Lett.* **2020**, *91*, 2141–2151. [CrossRef]
43. Ravilious, K. Data hint at quake forecasts Italian-earthquake analysis suggests possibility of predicting aftershocks of some quakes. *Nature* **2018**, *562*, 470–471. [CrossRef]
44. Ziv, A.; Rubin, A.M. Static stress transfer and earthquake triggering: No lower threshold in sight? *J. Geophys. Res. Solid Earth* **2000**, *105*, 13631–13642. [CrossRef]
45. Mildon, Z.K.; Toda, S.; Faure Walker, J.P.; Roberts, G.P. Evaluating models of Coulomb stress transfer: Is variable fault geometry important? *Geophys. Res. Lett.* **2016**, *43*, 12407–12414. [CrossRef]